

Annual Review of Materials Research

Shear Pleasure: The Structure, Formation, and Thermodynamics of Crystallographic Shear Phases

Albert A. Voskanyan and Alexandra Navrotsky

School of Molecular Sciences and Center for Materials of the Universe, Arizona State University, Tempe, Arizona 85287, USA; email: avoskan3@asu.edu, alexandra.navrotsky@asu.edu

ANNUAL
REVIEWS **CONNECT**

www.annualreviews.org

- Download figures
- Navigate cited references
- Keyword search
- Explore related articles
- Share via email or social media

Annu. Rev. Mater. Res. 2021. 51:521–40

First published as a Review in Advance on
March 23, 2021

The *Annual Review of Materials Research* is online at
matsci.annualreviews.org

<https://doi.org/10.1146/annurev-matsci-070720-013445>

Copyright © 2021 by Annual Reviews.
All rights reserved

Keywords

crystallographic shear, extended defects, Magnéli phases, Wadsley-Roth, shear structure, shear energetics

Abstract

A renaissance of interest in crystallographic shear structures and our recent work in this remarkable class of materials inspired this review. We first summarize the geometrical aspects of shear plane formation and possible transformations in ReO_3 , rutile, and perovskite-based structures. Then we provide a mechanistic overview of crystallographic shear formation, plane ordering, and propagation. Next we describe the energetics of planar defect formation and interaction, equilibria between point and extended defect structures, and thermodynamic stability of shear compounds. Finally, we emphasize the remaining challenges and propose future directions in this exciting area.

The infinite variety in the properties of the solid materials we find in the world is really the expression of the infinite variety of the ways in which the atoms and molecules can be tied together, and of the strength of those ties.

W.H. Bragg, "Concerning the Nature of Things"

INTRODUCTION

Today, one cannot agree more with Hoffmann's 1987 statement that "[s]olid state chemistry is important, alive, and growing" (1, p. 846). Once thought to be a saturated discipline, solid-state chemistry has blossomed radiantly, demonstrating unprecedented glory in the second half of the twentieth century, thanks to the rapid development of quantum mechanics and cutting-edge structure analysis tools such as electron microscopy, high-energy X-ray diffraction, neutron scattering, and solid-state nuclear magnetic resonance. The symbiosis of chemistry, physics, and crystallography and the unlimited possible combination of elements of the periodic table has resulted in discoveries of novel solid materials (e.g., nanostructures, ordered porous solids, an endless array of perovskites, high-entropy alloys and oxides, MXenes) with remarkable physicochemical properties, leading to applications such as superconductors, energy storage devices, catalysts, magnets, and phosphors, which stretch the preexisting boundaries of science and technology.

The ultimate goal of practical utilization of materials largely depends on being able to produce them reproducibly with desired functionalities for a given specific application. The properties of solid materials can be tuned by their elemental composition. Small deviations from stoichiometry unavoidably generate defects in the crystal structures, significantly altering the properties of the solid. By controlling the nature, concentration, and mobility of such defects, the reactivity, sintering, and many properties (including electrical and magnetic properties) of solids can be tailored to a great degree (2). The formation of point defects (vacancies, interstitials, or defect clusters) is not the only route to modification of the solid composition. The partial reduction of certain transition metal oxides (such as WO_3 , MoO_3 , TiO_2 , Nb_2O_5 , and V_2O_5) leads to the formation of extended planar defects or shear planes rather than point defects (3). Any planar boundary in a crystal leads to a local rearrangement in coordination and to a local change in composition. If shear planes are in variable numbers and randomly distributed, a crystal with variable composition is generated. In contrast, if shear planes are periodic, a homologous series of new phases, each characterized by the separation between the planes defining a fixed composition, can be obtained (4). The formation of shear planes at different periodicities by the elimination of anion vacancies results in a new class of fascinating materials known as crystallographic shear (CS) phases or structures. A constellation of eminent scientists and pioneers—including Magnéli, Wadsley, Anderson, Roth, Bursill, Hyde, Andersson, Catlow, O'Keeffe, Eyring, Tilley, Iijima, Matzke, and others—performed extensive seminal experimental and theoretical studies of formation and characterization of these materials between 1950 and 1980. In particular, the pioneering work of Magnéli on shear structures of reduced tungsten and molybdenum oxides (Magnéli phases), the subsequent concept of block structures developed by Wadsley, and high-resolution electron microscopy by Iijima were revolutionary for progress in solid-state chemistry. The work of Murphy and Cava at Bell Laboratories allowed for the utilization of block-type CS structures for reversible insertion of Li ions at room temperature (5–11). After almost 30 years of relative calm in the field, the work of Han, Goodenough, and colleagues (12, 13) demonstrating the excellent electrochemical performance of the TiNb_2O_7 shear phase rekindled active research in shear phases. As a result, a vast number of Wadsley-Roth shear phases were recently synthesized and tested as intercalating anode materials in lithium ion batteries due to their high volumetric capacities, high safety, fast charging, rapid lithium transport, and buffered volume expansion (14–27).

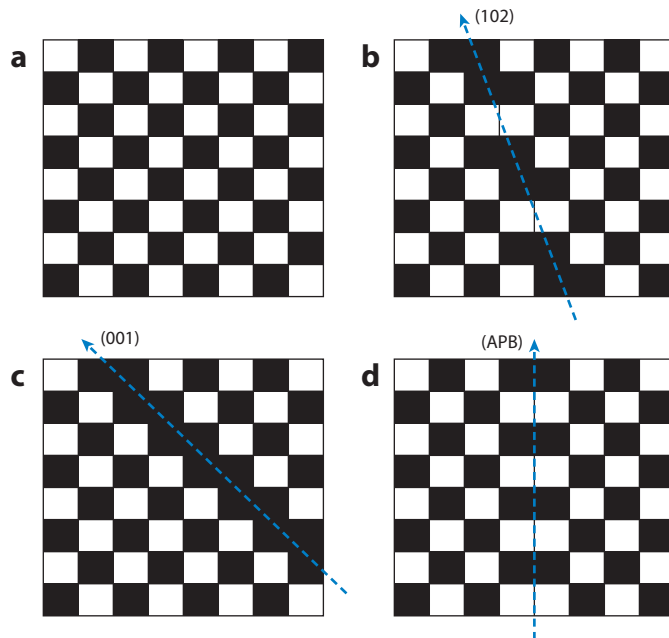


Figure 1

Schematic representation of crystallographic shear plane formation (Wadsley defect) in ReO_3 -type structure. Black squares represent metal-oxygen octahedra projected along $[001]$, and white squares denote empty tunnels. (a) A perfect ReO_3 structure of corner-sharing octahedra. (b,c) Generation of (b) (102) and (c) (001) crystallographic shear planes by application of the $R = \frac{1}{2}[10\bar{1}]$ displacement vector. (d) The antiphase boundary (APB) $(101)\frac{1}{2}[10\bar{1}]$. Blue dashed arrows represent the crystallographic shear plane.

This article reviews CS plane structure, mechanisms of formation, and energetics. We discuss ReO_3 and rutile-based Magnéli phases, Wadsley-Roth block structures, and the formation of CS in perovskites. We conclude this article by providing our future perspectives on these materials.

CRYSTALLOGRAPHIC SHEAR PLANE TOPOLOGY

Reduction of anion content in certain transition metal-containing compounds with a ReO_3 or rutile structure generates anion vacancies that undergo elimination after local reconstruction of the crystal to form translational CS planes. This process can be visualized as removing anion sites along the crystallographic plane, which leads to the compression of neighboring coordination polyhedra as a result of a shear operation that connects two anion sites (28–32). **Figure 1** illustrates, through a chessboard model, a simple schematic of CS plane formation in the ReO_3 structure. The aristotype ReO_3 structure is composed of an infinite three-dimensional arrangement of octahedra MO_6 , linked together by corner sharing (**Figure 1a**). A loss of oxygen from this structure changes the corner-sharing connectivity of the octahedral units. Along the defined CS planes, the octahedra share edges (**Figure 1b,c**) instead of sharing vertices as in the parent structure, so the number of oxygen atoms is reduced, resulting in nonconservative defects. The resulting extended defects are the CS planes, which at relatively low anion deficiency are aligned along (102) and at very high defect concentrations are aligned along (001), as shown in panels b and c of **Figure 1**, respectively. Another pictorial way of demonstrating CS plane formation is the paper and scissor model (33). A

Table 1 Relationship between crystallographic shear (CS) plane topology and stoichiometry of cubic crystals (37)

CS plane	Formula of homologs	Number of oxygen atoms lost per unit	CS plane spacing, d_{hkl}
{102}	M_nO_{3n-1}	1	$(n - 1/2)a/\sqrt{5}$
{103}	M_nO_{3n-2}	2	$(n - 1)a/\sqrt{10}$
{104}	M_nO_{3n-3}	3	$(n - 3/2)a/\sqrt{17}$
{10 <i>l</i> }	$M_nO_{3n-(l-1)}$	$l - 1$	$(n - l + 1/2)a/\sqrt{l^2 + 1}$

cut along the {*b*0*l*} crystal plane will artificially duplicate the oxygen atoms, and half of these atoms should be eliminated to accommodate point defects. Oxygen reduction takes place by shearing the cut structure with respect to the other part by a displacement vector of $R = \frac{1}{2}[10\bar{1}]$, which corresponds to the proportion of lattice translation of the original structure (31, 34). The shear operation leads to a composition change since the oxygen-to-metal (O/M) ratio is higher in the CS plane than the one-third ratio in the MO_3 structure. If the displacement vector is parallel to the plane, the resulting planar defect is conservative and does not lead to the elimination of oxygen atoms. In this case, the shear operation results only in antiphase boundary (APB) formation (Figure 1*d*), with no change in composition.

With the help of the APB, all CS planes in the ReO_3 structure can be resolved into the sum of two components, one nonconservative and the other conservative, namely the most oxygen-deficient CS plane $(001)\frac{1}{2}[10\bar{1}]$ and the APB $(101)\frac{1}{2}[10\bar{1}]$ (35, 36). Hence, one can write

$$\begin{aligned}(b0l) &= p(001) + q(101) \\ &= (q, 0, p + q),\end{aligned}\tag{1}$$

so that $q = b$, $p = l - b$, and $(b0l) = (l - b)(001) + b(101)$. ($p + q$) is the number of edge-sharing pairs of octahedra in the unit length of the CS plane, which are arranged in q separate groups. In the simplest case of $q = 1$, (102) shear planes are produced by $p = 1$, (103) planes by $p = 2$ and $q = 1$, and (001) when $p = \infty$ and $q = 1$, showing that with an increase in p , the CS plane orientation changes discontinuously. Thus, (105) can be represented as

$$(105) = 4(001) + 1(101)\tag{2}$$

and implies that the structural unit of the CS plane consists of groups of five pairs of edge-sharing octahedra separated by voids in the structure. If $q > 1$, an infinite number of intermediate CS planes can form. For example, if $q = 3$ and $p = 4$, the CS plane is parallel to (307) and made up of two units of (102) plus one of (103) that alternate in the structure. The formation of four edge-sharing octahedra in the {102} CS plane eliminates one oxygen atom, six edge-sharing octahedra remove two oxygen atoms in the {103} plane, and in general $(l - 1)$ oxygens are removed in the {10*l*} plane (37). If the {10*l*} CS planes form an ordered array in the ReO_{3-x} crystal, homologous series of ordered oxides with the general formula $M_nO_{3n-(l-1)}$ (with n and l integers and where n is the number of coordination octahedra in layers between neighboring CS planes) can result. Homologous series of oxides with the general formula $(W, Mo)_nO_{3n-1}$ and Ti_nO_{2n-1} are known as Magnéli phases (38–45). As the separation between CS planes changes (d_{hkl}), the stoichiometry and the formula of an oxide change. The distance between the nearest CS planes also significantly affects the distortions in MO_6 octahedra. **Table 1** shows the relationships between CS plane topology and stoichiometry (37).

Through simultaneous performance of two almost orthogonal and intersecting shear operations, namely $(\frac{1}{2})[011]/(b0l)$ with $l > b$ and $(\frac{1}{2})[\bar{1}10]/(b'0l')$ with $b' > l'$, so-called block structures

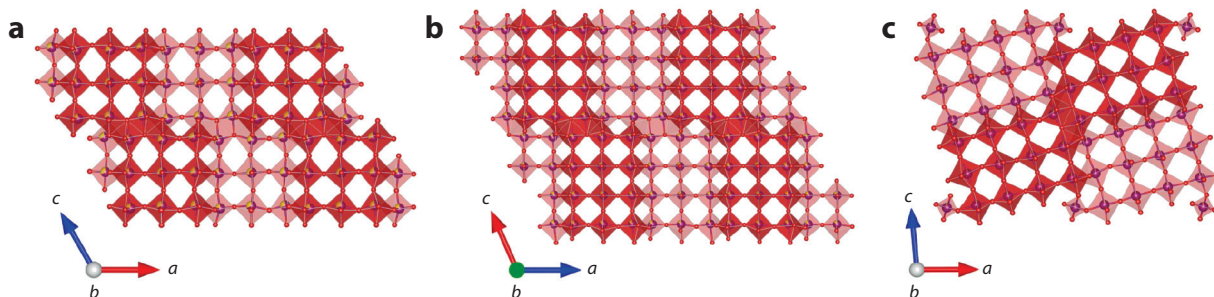


Figure 2

Crystal structures of (a) TiNb_2O_7 , (b) $\text{TiNb}_5\text{O}_{14.5}$, and (c) $\text{TiNb}_{24}\text{O}_{62}$ viewed along the b axis, with visible 3×3 octahedral blocks, 3×4 octahedral blocks, and 3×4 octahedral blocks + 0.5 tetrahedral blocks, respectively. Figure adapted with permission from Reference 53.

or Wadsley-Roth phases are derived from the ReO_3 aristotype (45–52). Their crystal structure is built up from rectangular blocks of ReO_3 measuring ($m \times n$) octahedra of finite sizes in two dimensions but infinite in the third dimension. These blocks condense upon themselves by edge sharing in such a way that tetrahedrally coordinated atoms may, or may not, be present at the junctions (**Figure 2**). Blocks are separated by CS planes in two directions at right angles. In adjacent blocks, octahedrally coordinated cations are at different levels and sheared by half an octahedron, so the blocks are connected by edge sharing between their peripheral octahedra. Blocks at the same level can be connected by edge sharing or joined indirectly through cations in tetrahedral sites that are formed between the blocks to fill the voids in the structure (53). The O/M ratio dictates the block size, and compounds with larger block size form if the O/M ratio is high, as a high ratio allows for more corner-shared octahedra. The changes in composition can be accommodated by variation of block size, block connectivity, and intergrowth of different block structures that change the number of anion sites removed by octahedral edge sharing. If the anions are not completely removed in the plane, the remaining ones can increase the cation coordination number from six to seven, converting octahedra into pentagonal bipyramids.

Analogous formation of CS planes occurs in structures derived from rutile (30, 36, 54, 55). The tetragonal rutile structure is composed of chains of edge-shared $[\text{TiO}_6]$ octahedra, and the chains themselves are joined by corner sharing so that the orientation of neighboring chains differs by $\pi/2$ radians. As in ReO_3 structures, compositional change in tetragonal rutile structures can be accommodated by coordination changes. Because of the more complex structure of rutile, a simple depiction of CS plane formation by the chessboard model is not possible, so the structure is commonly described as an ideal hexagonal close-packed (hcp) framework of oxygens, with cations occupying alternating rows of octahedral interstices (**Figure 3a**). Performing a shear operation with a displacement vector of $\frac{1}{2}[0\bar{1}1]$ parallel to the (011) plane produces APB (**Figure 3b**) without a change in stoichiometry, and each $[\text{TiO}_6]$ octahedron shares six corners and two edges. The step resulting in APB is denoted by the \blacktriangle symbol, and such a trajectory of planes can be represented as

..... $\blacktriangle\blacktriangle\blacktriangle\blacktriangle\blacktriangle\blacktriangle\blacktriangle\blacktriangle\blacktriangle\blacktriangle\blacktriangle\blacktriangle$

The same displacement vector operating on (121) eliminates oxygen sites from the rutile structure, and the different type of step that occurs is denoted by \blacktriangledown , as shown in **Figure 3c**. The CS plane with such a sequence of steps can be displayed as

..... $\blacktriangledown\blacktriangledown\blacktriangledown\blacktriangledown\blacktriangledown\blacktriangledown\blacktriangledown\blacktriangledown\blacktriangledown\blacktriangledown\blacktriangledown\blacktriangledown$

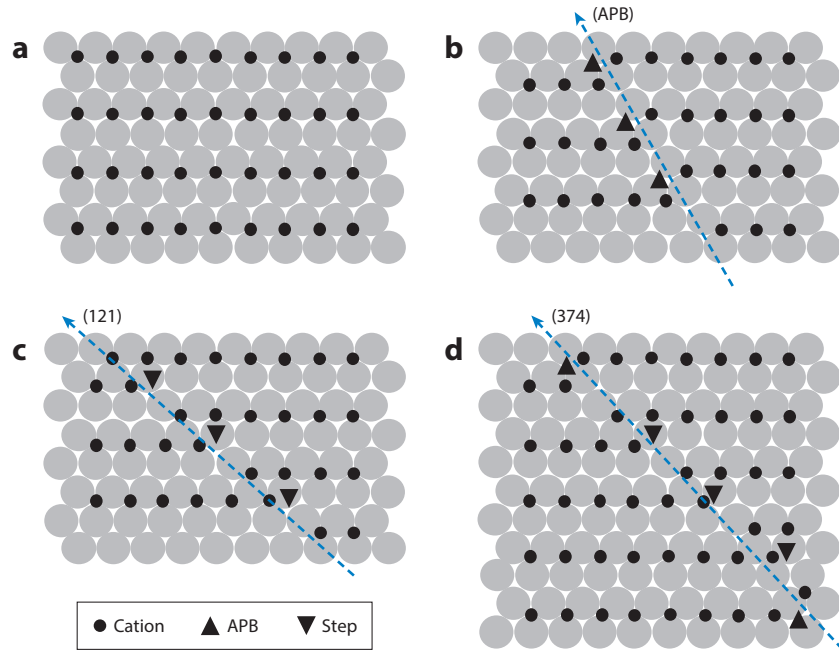


Figure 3

Schematic illustration of idealized (100) layers of (a) rutile, (b) an antiphase boundary plane (APB) $(011)\frac{1}{2}[0\bar{1}1]$, (c) a crystallographic shear (CS) plane $(121)\frac{1}{2}[0\bar{1}1]$, and (d) $(374)\frac{1}{2}[0\bar{1}1]$. The displacement vector $R = \frac{1}{2}[0\bar{1}1]$. Blue dashed arrows represent CS planes. Figure adapted from Reference 36.

Generally, at higher defect concentrations, the direction of the CS plane changes according to the following equation:

$$\begin{aligned} (bkl) &= p(121) + q(011) \\ &= (p, 2p + q, p + q). \end{aligned} \quad 3.$$

Thus, each CS plane is an ordered intergrowth of the component units of a (121) CS plane and a (011) APB with possible values for $p/q = 1, 2, 3, 4, \infty$. All the members of ordered (bkl) structures have M_nO_{2n-p} stoichiometries (where n and p are integers), and at $p = \infty$, the general formula degenerates to the M_nO_{2n-1} homologous series. The sequence of steps strictly depends on p and q values, and extremes of the series are the (121) and (132) planes. When $q/p = \infty$, the steps form a $\dots\blacktriangle\blacktriangle\blacktriangle\dots$ trace, as in (001) APB (Ti_nO_{2n}), and for $p/q = \infty$, a $\dots\blacktriangledown\blacktriangledown\blacktriangledown\dots$ trace forms (121). The combination of $(q\blacktriangle + p\blacktriangledown)$ creates an unlimited number of possible intermediate orientations (Table 2).

By performing a regular $(011)\frac{1}{2}[0\bar{1}1]$ APB operation at every alternate (001) anion plane, an orthorhombic α - PbO_2 structure can be generated, as shown in **Figure 4a** (55). This structure is a high-pressure polymorph of rutile, and the CS planes appear to kinetically allow the structure to be quenched to atmospheric pressure as a metastable phase. The α - PbO_2 structure has the same hcp array of oxygen atoms as in rutile, but with a zigzag ordering of the chains of edge-shared cation-anion octahedra. This ordering increases the structure's density. The equilibrium pressure for the rutile-to-orthorhombic α - PbO_2 phase transition is 6 ± 2 GPa at 294 K (56). The enthalpy of transformation obtained by high-temperature calorimetry is -3.18 ± 0.71 kJ/mol, and the change in volume associated with the transformation is +2.8%.

Table 2 Possible crystallographic shear (CS) planes formed from intergrowth of the (011) antiphase boundary and (121) planes of rutile-based structures

CS plane	p	q	Sequence of steps
(011)	0	1	▲▲▲▲▲▲▲
(121)	1	0	▼▼▼▼▼▼▼
(132)	1	1	▲▼▲▼▲▼▲
(253)	2	1	▲▼▼▲▼▼▲
(374)	3	1	▲▼▼▼▲▼▼▼
(154)	1	3	▲▲▲▼▲▲▲▼

The corundum structure can be created by a $(001)\frac{1}{2}[0\bar{1}1]$ shear operation (**Figure 4b**), and if the operation is repeated twice, a hexagonal (0001) layer of a NiAs structure forms. Unlike the case of inserting extra cations into empty octahedral sites of rutile, arranging them in this manner alleviates the strain arising from unfavorable cation repulsion.

Hyde et al. (36) discussed in detail CS structures with more exotic coordination polyhedra, including derivatives of TmCl_3 and Cu-Au alloys (57, 58). Furthermore, by intercalation of foreign atoms at APBs, some oxyhydroxides can also be considered as rutile derivatives (36).

ReO_3 structures can be considered as perovskites (ABX_3) with vacant cuboctahedral A sites. Anions and anion vacancies in $ABX_{3-\delta}$ perovskite structures can be arranged in different ordered patterns, and their ordering strongly depends on the properties of A and B cations. Abakumov et al. (59, 60) demonstrated that, by performing shear operation with a combination of two displacement vectors as $R = \frac{1}{2}[110] + \frac{1}{3}[001]$ on an $A_2\text{Fe}_2\text{O}_5$ anion-deficient perovskite, a CS structure can be generated. Similar to the case of block structures, the production of CS planes modifies the linkage of octahedra, but without changing the coordination number of B cations. In particular, a nonconservative $\frac{1}{2}[110]$ shear vector applied to the (101) plane removes some of the oxygen atoms (**Figure 5a**) due to a change from corner sharing to edge sharing. The oxygen atoms that are not eliminated by the shear operation cannot remain in the structure due to the extremely short metal-oxygen distances.

The resulting $(\bar{1}01)\frac{1}{3}[001]$ displacement relaxes the structure, transforming FeO_6 octahedra into FeO_5 tetragonal pyramids (**Figure 5c**). **Figure 5d** shows a [010] HAADF STEM (high-angle annular dark-field scanning transmission electron microscopy) image of $\text{Pb}_2\text{Fe}_2\text{O}_5$. **Figure 5e** schematically shows the resulting atomic arrangement of the cations. The pyramid chains have $A_2\text{Fe}_2\text{O}_4$ composition, and adding them to perovskites with layer thickness n results in a homologous series with planar interfaces having $A_{2+n}\text{Fe}_{2+n}\text{O}_{4+3n}$ composition. $\text{Pb}_2\text{Fe}_2\text{O}_5$ has a large

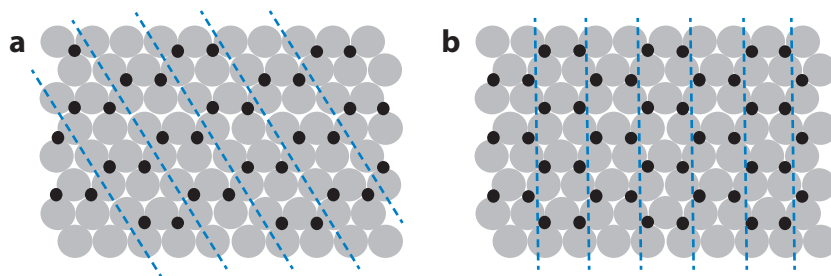


Figure 4

(a) A (100) layer of orthorhombic $\alpha\text{-PbO}_2$. (b) A (0001) layer of corundum. Blue dashed lines represent crystallographic shear planes. Adapted from Reference 36.

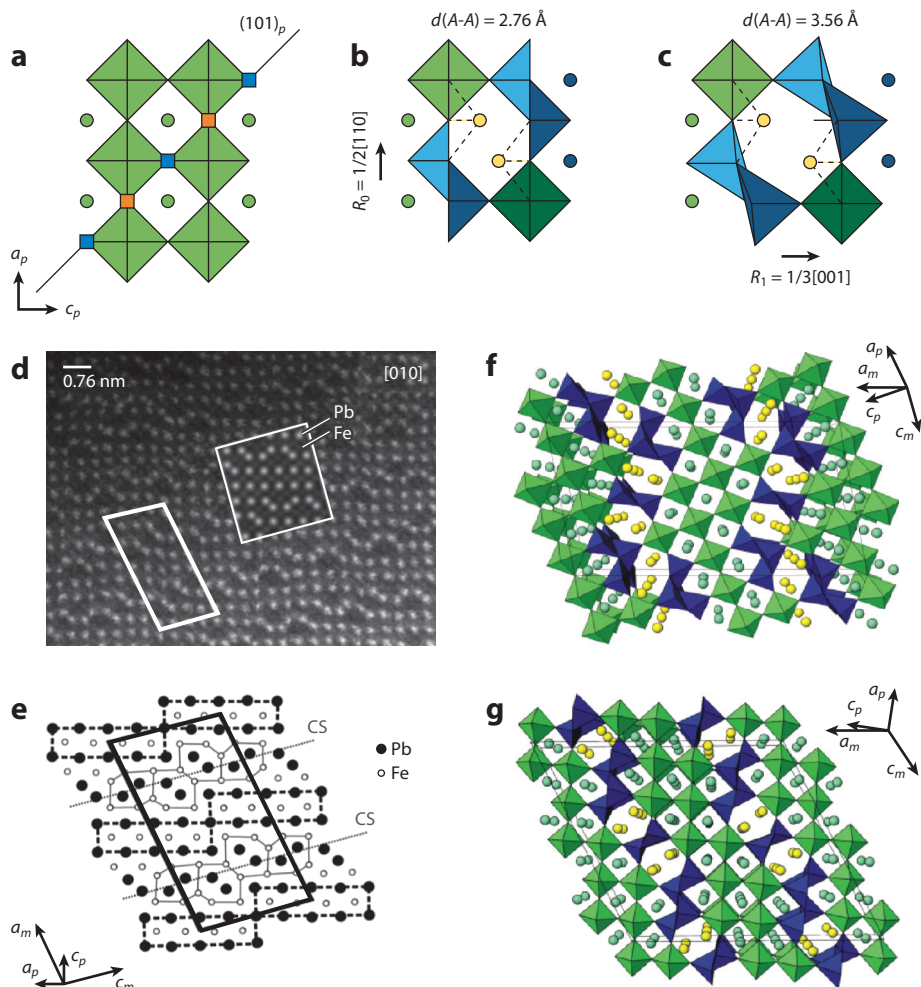


Figure 5

(a,b) Creation of oxygen vacancies (orange squares) (a) by a $(\bar{1}01)\frac{1}{2}[110]$ shear vector converting FeO_6 into FeO_5 pyramids (b). Oxygen atoms that are not eliminated by the shear operation are denoted by blue squares. Edge-shared polyhedra are shown in blue in panel b. (c) The $(\bar{1}01)\frac{1}{3}[001]$ relaxes the structure, increasing the distance between A-type cations. In panels a–c, FeO_6 octahedra are light green, FeO_5 pyramids are light blue, displaced FeO_5 octahedra are dark green, A-type cations after relaxation from displacement are yellow circles, A-type cations before displacement are green circles, and A-type cations after displacement are blue circles. (d) [010] HAADF STEM (high-angle annular dark-field scanning transmission electron microscopy) image of $\text{Pb}_2\text{Fe}_2\text{O}_5$. The brighter spots on the unfiltered [010] HAADF STEM image of $\text{Pb}_2\text{Fe}_2\text{O}_5$ correspond to Pb columns, whereas the dimmer spots correspond to the projection of Fe columns. The monoclinic unit cell is outlined in thick white lines, and a simulation of the image is outlined in thin white lines. (e) Arrangement of columns of Pb and Fe atoms in $\text{Pb}_2\text{Fe}_2\text{O}_5$. The monoclinic unit cell is outlined by thick solid lines, the perovskite blocks are outlined by thick dashed lines, the six-sided channels are outlined by thin solid lines, and the crystallographic shear (CS) planes are indicated by thin dotted lines. (f,g) Perspective views of the (f) $\text{Pb}_{15}\text{Fe}_{16}\text{O}_{39} \frac{1}{2}[110](104)_p$ and (g) $\text{Pb}_{18}\text{Fe}_{20}\text{O}_{48} \frac{1}{2}[110](305)_p$ CS structures. FeO_5 tetragonal pyramids are blue, FeO_6 octahedra are green, Pb atoms in the six-sided tunnels are yellow circles, and A-type cations located in the cavities of perovskite blocks are green circles. Panels a–c, f, and g adapted with permission from Reference 60. Panels d and e adapted with permission from Reference 59.

variety of CS structures (**Figure 5f,g**). Application of other conservative or nonconservative shear operations to the $(\bar{1}01)$ plane can generate anion-deficient perovskite structures with different compositions (61–63).

In contrast to the case of anion-deficient perovskites, a CS structure was also reported in layered perovskites $\text{La}_4\text{Sr}_{n-4}\text{Ti}_n\text{O}_{3n+2}$ with oxygen excess (64, 65). At $n < 7$, layered phases form, and consecutive blocks are joined via CS of oxygen-rich planes. With increasing n , extended defects become more irregularly spaced, and at $n > 11$, shear structures disappear, and only oxygen-rich defects are randomly distributed within the structure. The excess oxygen beyond ABO_3 stoichiometry is located in oxygen-rich defect regions and is not compensated by A -site cation vacancies.

MECHANISMS OF CRYSTALLOGRAPHIC SHEAR PLANE FORMATION

The general mechanism of shear plane formation has been the subject of intense controversy and remains somewhat enigmatic. Several different homogeneous and heterogeneous formation models that can explain specific cases have been proposed, but none of these mechanisms can explain CS plane formation for the whole class of materials. The mechanism proposed by Gado (66, 67) assumes that a crystal loses oxygen, producing oxygen vacancies. These vacancies then order inside the crystal, forming walls across which the crystal shears, annihilating vacant sites and generating a shear plane (schematically illustrated in **Figure 6a**). Repetition of this process results in parallel CS planes that divide the original structure into slabs. For his model, Gado considered the reaction $20\text{WO}_3 \rightarrow \text{W}_{20}\text{O}_{58} + \text{O}_2$, for which a high anion vacancy concentration of 3.3% is needed before lattice condensation takes place (31). However, experiments have shown that the formation of shear plane occurs even at ten-times-lower defect concentrations. Such a large concentration of vacancies in the face-centered-cubic ReO_3 structure is very unlikely, if not impossible. In addition, this model does not explain CS plane ordering and rearrangement.

Anderson & Hyde (34, 68) proposed another mechanism (the dislocation model) suggesting that the elimination of oxygen from the crystal creates random oxygen vacancies that then order, forming planar disks. At a critical defect concentration, which is much lower than that required for Gado's model, the flat disk collapses, producing a nucleus of a CS plane enclosed by a partial dislocation loop. Due to elastic stress, the dislocations act as vacancy sinks, trapping other vacancies by a loop that diffuses from the bulk to this region. Consequently, the CS plane propagates to the intersection with the crystal surface. **Figure 6b** shows this mechanism. Evidence for this dislocation

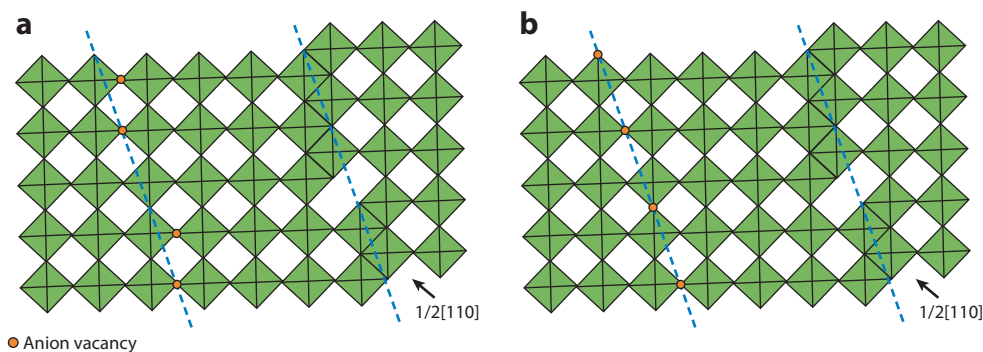


Figure 6

The (a) Gado and (b) Anderson-Hyde dislocation models for the generation of crystallographic shear planes (blue dashed lines) in an ReO_3 -type structure. Adapted from Reference 33.

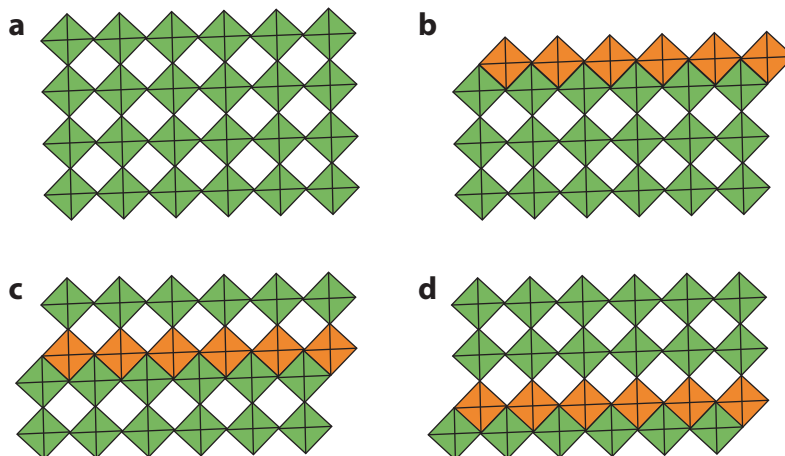


Figure 7

The Andersson-Wadsley mechanism of cooperative migration. (a) Perfect ReO₃ structure of corner-sharing octahedra (green). (b) Formation of a shear plane. (c,d) Propagation of the shear plane. The shear plane is shown in orange.

mechanism for the nucleation and growth of CS planes is provided by the reduction of MoO₃ with an electron beam (69), NbO₂F (70), and Nb₃O₇F (71). The dislocation mechanism assumes that vacancies, and not cation interstitials, compose the majority of point defects, but this assumption has been debated. Other complex nucleation mechanisms based on cation interstitials with cation sublattice rearrangement have also been proposed. In the cases of WO_{3-x} and MoO_{3-x}, evidence for nucleation of vacancy dislocation loops was obtained, while for TiO_{2-x}, cation interstitials were found via drawing Burgers's circuit onto HRTEM images (72). Dislocation-limited CS planes have been occasionally observed, mostly in materials close to stoichiometric composition. The advantage of this model is avoiding high vacancy concentration. However, while explaining CS plane propagation, this model does not describe how CS planes order and defects migrate to produce intermediate phases.

Andersson & Wadsley (73) proposed the cooperative migration model, which involves CS plane formation on the crystal surface without the involvement of point defects. The CS plane is produced through the reduction of oxygen at the surface, liberating oxygen atoms into the gas phase (Figure 7a). Afterward, metal-oxygen rows cooperatively move to adjacent empty sites by leaving their original positions (Figure 7b,c). The Wadsley defects formed can migrate into the next row of interstitials by successive cooperative steps, thus diffusing deeper into the interior of the crystal (Figure 7d).

The net effect is the unidirectional propagation of planar defects through the crystal under a stress gradient. This mechanism can be used to explain why perovskites (*ABO*₃) having an ReO₃ structure with filled *A* sites do not form related CS structures, since cation diffusion is hindered when cuboctahedral *A* sites are occupied (73). Migration of Wadsley defects should not be confused with lattice oxygen diffusion in oxides; the latter occurs because of a concentration gradient and results in random oxygen diffusion in all possible directions. However, the direct formation of Wadsley defects inside the crystal is excluded in this model, which disagrees with experimental results. Hyde & Bursill (31) noted that, to form a single CS plane inside a structure, a vast number of ions (e.g., 50% of Ti⁴⁺ in TiO₂) must migrate from the surface, and such migration may not be energetically favorable at low concentrations of CS planes.

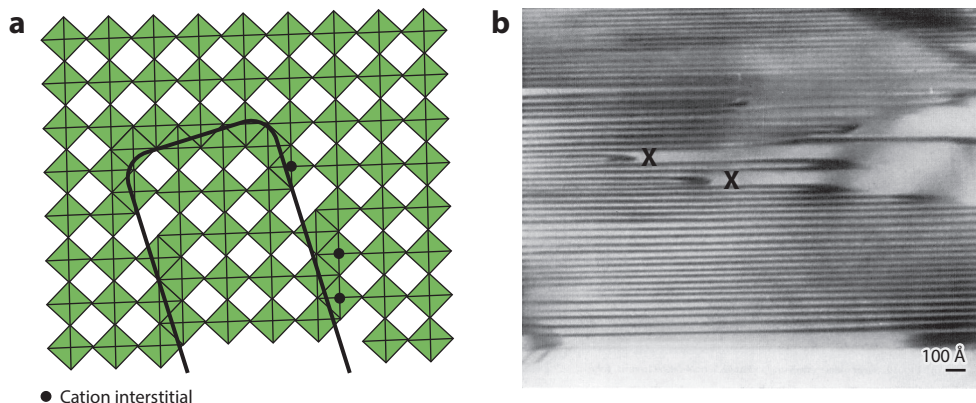


Figure 8

(a) Hairpin model proposed by Van Landuyt & Amelinckx (75). Thick black lines denote a hairpin loop. (b) TEM image demonstrating isolated hairpins (marked by X) in an irregular sequence of crystallographic shear planes in TiO_{2-x} . Figure adapted with permission from Reference 75.

O'Keeffe (74) pointed out that the Anderson-Hyde mechanism explains the formation and growth of Wadsley defects, while the Andersson-Wadsley model elucidates the formation and propagation of those defects. Another mechanism related to the Andersson-Wadsley model is the hairpin propagation model suggested by Van Landuyt & Amelinckx (75) (**Figure 8a**). The difference between these two mechanisms is that the Van Landuyt & Amelinckx model does not assume the cooperative movement of the whole row, but rather only some fraction of it. This model explains the formation, the lateral displacement, and the longitudinal growth of CS planes. Hairpin-shaped CS planes have been observed only in TiO_{2-x} thin foils with a clearly visible (by TEM) hairpin tip in which all cooperative jumps and interstitial propagations take place (**Figure 8b**). In reality, depending on thermodynamic parameters (such as temperature, pressure, and composition), all these mechanisms can operate simultaneously. Although these models can explain some cases, a universal mechanism for Wadsley defect formation, growth, and migration should be formulated with the help of modern computational capabilities.

SHEAR PLANE ENERGETICS

Although the energetics of point defect formation have been extensively studied, little is known about the energetics of planar defect formation and interaction. The intriguing fundamental questions are why these defects form, what is the thermodynamic price of formation, why they form only in special cases and not more generally, whether they coexist with point defects, and how extended defects interact with each other to produce long-range shear plane ordering.

Merritt & Hyde (76) performed accurate equilibrium thermodynamic measurements on TiO_x over a wide composition range ($1.66 \leq x \leq 2.00$) and determined the partial molar free energy of oxygen under precisely controlled $\text{H}_2 + \text{H}_2\text{O}$ gas buffers. They found that the composition range consists of five distinct regions. At $1.98 \leq x \leq 2.00$, mainly lamellae of ordered (132) CS planes are distributed in a rutile structure. With a further reduction, the $1.93 \leq x \leq 1.98$ region consists of (132) phases with very small composition intervals between neighboring ordered phases. The $1.90 \leq x \leq 1.93$ region is populated by a continuous array of ordered or partially ordered phases, and CS planes lie between (121) and (132). Thus, crystals within this region consist of coherent domains resulting from an ordered intergrowth of (121) and (132) planes at different proportions.

Importantly, changes in composition take place by changing the orientation rather than the density of the shear planes. In the $1.73 \leq x \leq 1.90$ region, (121) CS phases form, and when $1.66 \leq x \leq 1.73$, Ti_3O_5 coexists with Ti_4O_7 . The thermodynamic results show that complete equilibrium is not attainable with the very wide hysteresis loop observed over most of the composition range studied. These results indicate that in the TiO_2 system, another phase starts to appear before the next nearest phase in the series completely forms.

The generation of vacancies is usually an energetically expensive process and typically in the range of 1,500–2,000 kJ/mol for rutile and fluorite oxides (77–79). Thus, vacancy annihilation must be strongly exothermic. On the basis of this logic, the formation of shear planes should be energetically favorable relative to point defects and should be a more commonly observed type of defect. However, the production of CS shortens metal-metal distances and leads to electrostatic repulsions between metal atoms (78, 79). As a result, the formation of CS structures is allowed only when the exothermic energy of extended defect formation exceeds the endothermic Coulombic cation repulsion.

The reduction of repulsion energy in shear planes has been explained by metal atom relaxations away from the planes (78–82). The lattice energy calculations for perfect Ti_5O_9 , in which Ti atoms occupy the same sites as in the ideal rutile structure, and for Ti_5O_9 , in which the Ti^{3+} cations close to the CS plane are displaced by 0.3 Å from the centers of the octahedra, show a 975 kJ/mol energy difference between the relaxed and initial structures. This large difference confirms that cation relaxation significantly stabilizes shear structures. Furthermore, if the reduction of TiO_2 results in a divalent cation instead of a tetravalent one, then shear plane formation is stabilized by an even larger 1,060 kJ/mol per removed oxygen ion (80). This higher value is also attributed to the reduction of repulsion energy with the decrease in cation valence. However, reduced titanium oxides are more likely to contain trivalent rather than divalent titanium. These results suggest that doping oxide with lower-valence cations may strongly enhance stability and may even result in CS structures that otherwise might not form. It has also been calculated that a reduction of either ionic radius or electronic polarizability of dopant cations increases the binding energy of doped cations to the shear plane, forming more stable structures (80). Additionally, the reduction of oxides generates conduction band electrons that can interact with shear planes, and shear plane–electron binding energies are in the range of 10–60 kJ/mol for Ti_4O_7 and Ti_5O_9 (78). These values are small compared to calculated relaxation energies but are sufficiently large to have a dramatic impact on the thermodynamics of the formation and electrical conductivity of crystals.

Interesting results were obtained for CS planes in reduced oxides with the ReO_3 structure (3). The calculated unrelaxed lattice energies follow the sequence of (102) > (103) > (104) > (001), with (001) plane defects being the most stable. However, after ion relaxation, the low-symmetry (102) shear plane becomes the most stable one, which is explained by more substantial lattice relaxation in the lateral and perpendicular directions around these defects. In the case of the (001) plane, which is restricted by symmetry, ion displacements are perpendicular only to the plane. Moreover, the energies of different relaxed planes differ by only 50–100 kJ/mol.

The relaxation theory is supported by Tilley's (82) empirical observations that shear planes form in those crystals that possess very high static dielectric constants, ϵ_0 . High ϵ_0 values can effectively screen Coulombic interactions between charged defects. Two contributions, the electronic and ionic polarizabilities of atoms, compose ϵ_0 . Materials with low ϵ_0 (<24) tend to form point defects, whereas those with high ϵ_0 (>100) form extended defects. For example, TiO_2 , which has a high value of $\epsilon_0 \sim 100$, forms planar defects, while isostructural SnO_2 , with $\epsilon_0 \sim 15$, forms only point defects (79). A high ϵ_0 value is generally attributed to the high-ionic-polarizability term arising from the displacement of cations from the centers of octahedra. This empirical correlation considers room temperature ϵ_0 value, but this value can become large for some materials at the

synthesis temperature. Therefore, the temperature dependence of ε_0 should be considered. In addition, the ionic and electronic contributions of atoms are related to the allowed lattice vibrations of crystals, and high ε_0 is associated with a very low frequency transverse optical phonon in the lattice (78, 81). Defects can alter local fields in some areas of the crystal, thus affecting the stability of low-optical-phonon modes. The existence of soft phonon modes in the crystal may favor the formation of planar defects over point defects (53), although there is no quantitative analysis to favor this point. We suggest that the vibrational density of states obtained from cryogenic heat capacity measurements and inelastic neutron scattering of various shear structures may help to analyze the validity of such correlations.

High ε_0 values are not the immediate reason for shear plane stabilization (78, 81). Large cation displacements take place in materials with high polarizability, lead to high ε_0 , and hence should allow for large cation relaxations along the shear plane. Both high ε_0 values and CS plane formation are related to large cation polarizabilities, and rather than one causing the other, both arise from the essential characteristics of the metal-oxygen potential. Interestingly, colossal ε_0 was also recorded in high-entropy oxides without a concrete explanation of its origin (83). We suggest that this high ε_0 value may also be related to possible large cation displacements in these materials.

Because the formation of CS planes eliminates point defects, another question is whether point defects and shear planes can coexist in the same crystal structure. Statistical mechanics was used to deduce that, for crystals containing shear planes, an equilibrium concentration of point defects, however small, must exist (3, 78). If oxygen vacancies (V_o) are the predominant point defects in TiO_{2-x} , the following defect equilibrium can be written:



The generated electrons are confined in the positively charged shear plane and released after its dissociation. The calculated free energy for Reaction 4 is approximately 200 kJ/mol and has been calculated by ignoring all lattice entropy terms and including only the configurational entropy associated with point defects (79). Then this energy value is used to calculate the extended/point defect equilibrium. The results show that a considerable concentration of oxygen vacancies ($\sim 10^{-3}$) is in equilibrium with shear planes above 1,000 K. Even at very small concentrations, point defects may still influence transport and thermodynamic properties. Importantly, at extremely small deviations from stoichiometry, $x \approx 0.003$, possible shear planes are dissociated into anion vacancies that aggregate into CS planes only when x exceeds this value. These results can be extended to ReO_3 structures, assuming vacancy formation on oxide reduction. Shear planes exist for $WO_{2.994}$ in the temperature range of 1,000–1,500 K (3). Electrical conductivity studies above 1,000 K reveal a sharp change in conductivity at the near-stoichiometric region of TiO_{2-x} (84). This conductivity change is best explained by the aggregation of anion vacancies into extended defects, implying that CS planes start to form at the $TiO_{1.99}$ composition. A dramatic change in conductivity at room temperature was also observed for the $La_{4n-4}Ti_nO_{3n+2}$ perovskite series at $n = 12$, and below this point, extended defects are converted into randomly distributed oxygen-rich defect clusters (65).

Above we discuss aspects related to the topology, mechanism, and energetics of shear plane formation. Another important feature of shear planes is their long-range ordering, which results in homologous series of shear compounds such as Magnéli and Wadsley-Roth phases. The ordering of CS planes emerges from defect interactions. With the embedding of more planes into the crystal, the shear planes move to minimize the total Gibbs energy. Stoneham & Durham (85) developed a theory that explains the interaction of planes in the ReO_3 structure. This theory is based on plane-plane elastic interactions with a negligible electrostatic contribution. The electrostatic interaction is insignificant because the positive charge of shear planes is locally balanced by

conduction band electrons. According to this theory, shear planes are represented as defect forces, and each individual plane exerts force on the elastic strain field of the neighboring plane. The continuum elasticity approach can be used to analytically evaluate the interaction energy between two planes. Categorically different results have been obtained for interaction energies of infinite arrays and separate pairs of CS planes. For infinite arrays of planes, a deep energy minimum at finite spacing was predicted; this minimum corresponds to a spacing of approximately four times the width of the repeating unit within each plane. Away from the minimum, the interaction energy increases significantly. Experimentally observed plane spacings for different reduced oxides are in good agreement with the minimum predicted by this theory. The interaction of a pair of planes as a function of spacing is much more complicated because the periodicity of an array cannot be applied. The calculated results indicate oscillatory interactions between isolated pairs of CS planes with a series of maxima and minima; however, no evidence of oscillatory plane interactions has been recorded to date.

Iguchi & Tilley (86) extended the continuum elasticity theory by considering the actual shear planes in WO_3 instead of the hypothetical (100) plane in the ReO_3 structure used in earlier work. They concluded that, if only one set of CS planes is considered, the obtained microstructure as revealed by TEM is in accord with the prediction of elastic strain theory. However, the sequence of planes observed after the reduction of WO_3 is not regulated by strain energy; otherwise, (001) planes would always be favored. Therefore, Iguchi & Tilley speculated that the formation of the CS plane is governed by cation-cation and cation-anion-cation bonding within the CS plane. Furthermore, cubic sets of planes such as (102), (103), and (001) become nonequivalent in the real WO_3 structure, leading to distortions of MO_6 octahedra. Magnéli (87) pointed out that these off-center displacements of metal atoms differ between homologs and may have a significant influence on the stability of certain members of homologous series. Using atomistic computer modeling, Cormack (88) obtained attractive interactions of shear planes even at large separations. The origin of this interaction was also ascribed to the displacement of octahedra between the CS planes generating elastic strain fields.

We recently demonstrated that Wadsley-Roth shear phases of the $\text{TiO}_2\text{-Nb}_2\text{O}_5$ pseudobinary system such as TiNb_2O_7 , $\text{TiNb}_5\text{O}_{14.5}$, and $\text{TiNb}_{24}\text{O}_{62}$ have positive enthalpies of formation from binary oxides (TiO_2 and Nb_2O_5), implying that they are entropy stabilized and stable only above some minimum temperature (53). The energetically metastable entropy-stabilized intermediate phases $\text{Ca}_3\text{Fe}_2\text{TiO}_8$ and $\text{Ca}_4\text{Fe}_2\text{Ti}_2\text{O}_{11}$ have also been observed in the $\text{CaTiO}_3\text{-Ca}_2\text{Fe}_2\text{O}_5$ (perovskite-brownmillerite) system (89). High-synthesis temperature creates cation disorder, and the configurational entropy arising from such disorder can thermodynamically stabilize shear structures against decomposition. In the $\text{TiO}_2\text{-Nb}_2\text{O}_5$ series, increasing concentrations of higher-valence Nb^{5+} cations in ternary compounds decrease the energetic stability of these phases with respect to their binary constituents ($\text{TiNb}_2\text{O}_7 > \text{TiNb}_5\text{O}_{14.5} > \text{TiNb}_{24}\text{O}_{62}$). Substitution of Ti^{4+} with higher-valence Nb^{5+} likely increases unfavorable cation-cation repulsions along the shear plane. These results are in harmony with Pauling's third rule, which states that if two anion polyhedra share edges, the stability of an ionic structure decreases since two central metal atoms have less separation. The observed energetics suggest that $\text{TiNb}_{24}\text{O}_{62}$ has extensive cation disorder, whereas TiNb_2O_7 and $\text{TiNb}_5\text{O}_{14.5}$ appear to be substantially more ordered. Indeed, Cheetham & Von Dreele (90) observed partial cation ordering in TiNb_2O_7 and $\text{TiNb}_5\text{O}_{14.5}$ through neutron diffraction. They found that Nb^{5+} cations prefer the centers of blocks, whereas Ti^{4+} cations occupy corner sites because of electrostatic interactions.

These CS phases and probably many others constitute a new and extensive class of entropy-stabilized oxides or high-entropy oxides (91) that are stable only at high temperature and in which positive enthalpies of formation are counterbalanced by large positive entropies arising

from cation disorder and not from CS. Our results demonstrate that entropy stabilization of these oxides is possible through the disorder of two cations rather than five or more cations (the latter quantity is commonly part of the definition of high-entropy materials) (91–95). Such entropy stabilization of energetically unfavorable materials was noted 50 years ago in spinels with disordered cation distributions (96, 97).

We anticipate that thermodynamic stabilization via configurational entropy of cation distributions is more common than previously realized, and many new families of entropy-stabilized compounds are waiting to be synthesized.

CONCLUSIONS AND PERSPECTIVES

In this review, we present the structural aspects, mechanisms, and energetics of CS plane formation in a condensed form to avoid being overly exhaustive. We realize that there is still much to be learned and discovered concerning this fascinating class of materials. A number of fundamental questions related to the formation and energetics of shear plane should be revisited and answered using the exceptional opportunities provided by modern high-resolution electron microscopy, computer simulations, and state-of-the-art instrumentation for precise evaluation of various physicochemical properties of interest, including the thermodynamics of formation and transformation.

In particular, in situ X-ray diffraction of precursor mixtures under controlled temperatures and pressures may provide distinctive structural details of shear plane formation in different systems. Furthermore, information regarding the phase formation and thermophysical properties of shear structures can be acquired through in situ high-energy X-ray diffraction studies of levitated samples, which eliminate problems of reaction with containers. High-temperature calorimetric studies of different shear phases based on rutile or ReO_3 structures are necessary to assess the general thermodynamic stability trends of these compounds.

Not only inorganic solids but also organic-inorganic hybrid materials, including metal organic frameworks (MOFs), crystallize in ReO_3 and other perovskite-related structures (98). In the latter, the oxygen atoms in ReO_3 are replaced by organic anions, and MOFs with the ReO_3 -type structure include formates, carboxylates, guanidates, azolates, and others. Anion vacancies in MOFs can be readily generated by doping or substitution of higher-valence cations with lower-valence ones. Therefore, the logical question is whether CS formation is possible in MOFs. To the best of our knowledge, there is no report on shear plane or Wadsley defect formation in MOFs, and we suggest that experimental and/or theoretical clarification regarding the feasibility of such formation is worth investigating. Interestingly, researchers recently detected clear evidence of nonrandom ordering of vacancy networks in a single crystal of Prussian blue analog (PBA) via X-ray diffuse scattering (99, 100). Furthermore, these investigators found a surprising diversity of diffuse scattering patterns for PBAs and demonstrated that ordering strictly depends on each crystal's chemical composition as well as on the conditions used for crystallization. Precise defect engineering is the next step to tailor properties of materials for specific applications.

Wadsley-Roth shear structures have been identified as promising high-performance anode materials for lithium ion batteries. Despite much structure performance-oriented research, there are few reports on computational modeling of lithium insertion mechanisms, the effect of cation disorder, and electronic structure change throughout the lithiation of shear phases. The main drawback of these compounds is their extremely low electronic conductivity, which significantly affects the rate capability. Therefore, the synthesis of novel CS structures with high electronic conductivity and excellent energetic stability is necessary to enhance the electrochemical performance of these

materials. Intrinsically metastable CS phases may demonstrate excellent activity in catalyzing/ photocatalyzing industrially important chemical reactions.

DISCLOSURE STATEMENT

The authors are not aware of any affiliations, memberships, funding, or financial holdings that might be perceived as affecting the objectivity of this review.

ACKNOWLEDGMENTS

The time to write this article has been made possible as a result of staying at home due to the COVID-19 pandemic. It is timely to quote, “Life isn’t about waiting for the storm to pass. . . . It’s about learning how to dance in the rain” (Vivian Greene). This work was supported by the US Department of Energy Office of Basic Energy Sciences, grant DE-FG02-03ER46053.

LITERATURE CITED

1. Hoffmann R. 1987. How chemistry and physics meet in the solid state. *Angew. Chem. Int. Ed.* 26:846–78
2. Mrowec S. 1978. On the defect structure of non-stoichiometric metal oxides. *Ceram. Int.* 4:47–58
3. Cormack AN, Jones RM, Tasker PW, Catlow CRA. 1982. Extended defect formation in oxides with ReO_3 structure. *J. Solid State Chem.* 44:174–85
4. Collongues R. 1993. Nonstoichiometry in oxides. *Progr. Cryst. Growth Charact. Mater.* 25:203–40
5. Murphy DW, Greenblatt M, Cava RJ, Zahurak SM. 1981. Topotactic lithium reactions with ReO_3 related shear structures. *Solid State Ionics* 5:327–30
6. Cava RJ, Santoro A, Murphy DW, Zahurak SM, Roth R. 1981. Structural aspects of lithium insertion in oxides: Li_xReO_3 and $\text{Li}_2\text{FeV}_3\text{O}_8$. *Solid State Ionics* 5:323–26
7. Cava RJ, Santoro A, Murphy DW, Zahurak SM, Roth R. 1982. The structure of lithium-inserted metal oxides: LiReO_3 and Li_2ReO_3 . *J. Solid State Chem.* 42:251–62
8. Cava RJ, Kleinman DJ, Zahurak SM. 1983. $\text{V}_{3.2}\text{W}_{1.8}\text{O}_{13}$ and studies of the V_2O_5 - WO_3 - VO_2 ternary system. *Mater. Res. Bull.* 18:869–73
9. Cava RJ, Murphy DW, Rietman EA, Zahurak SM, Barz H. 1983. Lithium insertion, electrical conductivity, and chemical substitution in various crystallographic shear structures. *Solid State Ionics* 9–10:407–12
10. Cava RJ, Murphy DW, Zahurak SM. 1983. Secondary lithium cells employing vanadium tungsten oxide positive electrode. *J. Electrochem. Soc.* 130:243–45
11. Cava RJ, Murphy DW, Zahurak SM. 1983. Lithium insertion in Wadsley-Roth phases based on niobium oxide. *J. Electrochem. Soc.* 130:2345–51
12. Han J-T, Huang Y-H, Goodenough JB. 2011. New anode framework for rechargeable lithium batteries. *Chem. Mater.* 23:2027–29
13. Han J-T, Goodenough JB. 2011. 3-V full cell performance of anode framework TiNb_2O_7 /spinel $\text{LiNi}_{0.5}\text{Mn}_{1.5}\text{O}_4$. *Chem. Mater.* 23:3404–7
14. Griffith KJ, Senyshin A, Grey CP. 2017. Structural stability from crystallographic shear in TiO_2 - Nb_2O_5 phases: cation ordering and lithiation behavior of $\text{TiNb}_{24}\text{O}_{62}$. *Inorg. Chem.* 56:4002–10
15. Griffith KJ, Wiaderek KM, Cibir J, Marbella LE, Grey CP. 2018. Niobium tungsten oxides for high-rate lithium-ion energy storage. *Nature* 559:556–63
16. Hu L, Luo L, Tang L, Lin C, Li R, Chen Y. 2018. $\text{Ti}_2\text{Nb}_{2x}\text{O}_{4+5x}$ anode materials for lithium-ion batteries: a comprehensive review. *J. Mater. Chem. A* 6:9799–815
17. Zhu X, Xu J, Luo Y, Fu Q, Liang G, et al. 2019. $\text{MoNb}_{12}\text{O}_{33}$ as a new anode material for high-capacity, safe, rapid and durable Li^+ storage: structural characteristics, electrochemical properties and working mechanisms. *J. Mater. Chem. A* 7:6522–32
18. Deng S, Zhang Y, Xie D, Yang L, Wang G, et al. 2019. Oxygen vacancy modulated $\text{Ti}_2\text{Nb}_{10}\text{O}_{29-x}$ embedded onto porous bacterial cellulose carbon for highly efficient lithium ion storage. *Nano Energy* 58:355–64

19. Kocer CP, Griffith KJ, Grey CP, Morris AJ. 2019. Cation disorder and lithium insertion mechanism of Wadsley-Roth crystallographic shear phases from first principles. *J. Am. Chem. Soc.* 141:15121–34
20. Deng Q, Fu Y, Zhu C, Yu Y. 2019. Niobium-based oxides toward advanced electrochemical energy storage: recent advances and challenges. *Small* 15:1804884
21. Yang Y, Zhu H, Xiao J, Geng H, Zhang Y, et al. 2020. Achieving ultrahigh-rate and high-safety Li⁺ storage based on interconnected tunnel structure in micro-size niobium tungsten oxides. *Adv. Mater.* 32:1905295
22. Griffith KJ, Grey CP. 2020. Superionic lithium intercalation through 2 × 2 nm² columns in the crystallographic shear phase Nb₁₈W₈O₆₉. *Chem. Mater.* 32:3860–68
23. Preefer MB, Saber M, Wei Q, Bashian NH, Bocarsly JD, et al. 2020. Multielectron redox and insulator-to-metal transition upon lithium insertion in the fast-charging, Wadsley-Roth phase PNb₉O₂₅. *Chem. Mater.* 32:4553–63
24. Bashian NH, Preefer MB, Milam-Guerrero J, Zak JJ, Sendi C, et al. 2020. Understanding the role of crystallographic shear on the electrochemical behavior of niobium oxyfluorides. *J. Mater. Chem. A* 8:12623–32
25. Zhang Y, Zhang M, Liu Y, Zhu H, Wang L, et al. 2020. Oxygen vacancy regulated TiNb₂O₇ compound with enhanced electrochemical performance used as anode material in Li-ion batteries. *Electrochim. Acta* 330:135299
26. Tao R, Yang G, Self EC, Liang J, Dunlap JR, et al. 2020. Ionic liquid-directed nanoporous TiNb₂O₇ anodes with superior performance for fast-rechargeable lithium-ion batteries. *Small* 16:2001884
27. Kocer CP, Griffith KJ, Grey CP, Morris AJ. 2020. Lithium diffusion in niobium tungsten oxide shear structures. *Chem. Mater.* 32:3980–89
28. Wadsley AD. 1958. Modern structural inorganic chemistry. *J. Proc. R. Soc. N.S.W.* 92:25–35
29. Wadsley AD. 1964. Inorganic non-stoichiometric compounds. In *Non-Stoichiometric Compounds*, Vol. 98, ed. L Mandelcorn, pp. 98–209. New York: Academic
30. Anderson JS, Tilley RJD. 1972. Crystallographic shear and non-stoichiometry. In *Surface and Defect Properties of Solids*, Vol. 1, ed. MW Roberts, JM Thomas, pp. 1–56. London: Chem. Soc.
31. Hyde BG, Bursill LA. 1970. Point, line, and planar defects in some non-stoichiometric compounds. In *The Chemistry of Extended Defects in Non-Metallic Solids*, ed. L Eyring, M O'Keeffe, pp. 347–74. Amsterdam: North Holland
32. Allpress JG. 1972. Crystallographic shear in WO₃·xNb₂O₅ (x = 0.03–0.09). *J. Solid State Chem.* 4:173–85
33. Van Landuyt J. 1974. Shear structures and crystallographic shear propagation. *J. Phys. Colloq.* 35:C7–53–63
34. Anderson JS, Hyde BG. 1967. On the possible role of dislocations in generating ordered and disordered shear structures. *J. Phys. Chem. Solids* 28:1393–408
35. Bursill LA, Hyde BG. 1972. CS families derived from the ReO₃ structure type: an electron microscope study of reduced WO₃ and related pseudobinary systems. *J. Solid State Chem.* 4:430–46
36. Hyde BG, Bagshaw AN, Andersson S, O'Keefe M. 1974. Some defect structures in crystalline solids. *Annu. Rev. Mater. Sci.* 4:43–92
37. Tilley RJD. 1976. The energy of crystallographic shear plane formation in reduced tungsten trioxide. *J. Solid State Chem.* 19:53–62
38. Magnéli A. 1953. Structures of the ReO₃-type with recurrent dislocations of atoms: 'homologous series' of molybdenum and tungsten oxides. *Acta Crystallogr.* 6:495–500
39. Hagg G, Magnéli A. 1954. Recent structure investigations of oxygen compounds of molybdenum and tungsten. *Rev. Pure Appl. Chem.* 4:235–49
40. Magnéli A. 1956. Some aspects of the crystal chemistry of oxygen compounds of molybdenum and tungsten containing structural elements of ReO₃ or perovskite type. *J. Inorg. Nucl. Chem.* 2:330–39
41. Andersson S, Collen B, Kuylenstierna U, Magnéli A. 1957. Phase analysis studies on the titanium-oxygen system. *Acta Chem. Scand.* 11:1641–52
42. Andersson S, Sundholm A, Magnéli A. 1959. A homologous series of mixed titanium chromium oxides Ti_{n-2}Cr₂O_{2n-1} isomorphous with the series of Ti_nO_{2n-1} and V_nO_{2n-1}. *Acta Chem. Scand.* 13:989–97
43. Marezio M, Dernier PD. 1971. The crystal structure of Ti₄O₇, a member of homologous series Ti_nO_{2n-1}. *J. Solid State Chem.* 3:340–48

44. Magnéli A. 1978. Non-stoichiometry and structural disorder in some families of inorganic compounds. *Pure Appl. Chem.* 50:1261–71
45. Wadsley AD. 1955. The crystal chemistry of non-stoichiometric compounds. *Rev. Pure Appl. Chem.* 5:165–93
46. Wadsley AD. 1961. Mixed oxides of titanium and niobium. II. The crystal structures of the dimorphic forms of $\text{Ti}_2\text{Nb}_{10}\text{O}_{29}$. *Acta Crystallogr.* 14:664–70
47. Roth RS, Wadsley AD. 1965. Multiple phase formation in the binary system $\text{Nb}_2\text{O}_5\text{--WO}_3$. II. The structure of the monoclinic phases $\text{WNb}_{12}\text{O}_{33}$ and $\text{W}_5\text{Nb}_{16}\text{O}_{55}$. *Acta Crystallogr.* 19:32–38
48. Andersson S. 1967. The description of non-stoichiometric transition metal oxides. A logical extension of inorganic crystallography. *Bull. Soc. Fr. Mineral. Cristallogr.* 90:522–27
49. Allpress JG, Wadsley AD. 1969. Multiple phase formation in the binary system $\text{Nb}_2\text{O}_5\text{--WO}_3$. VII. Intergrowth of $\text{H--Nb}_2\text{O}_5$ and $\text{WNb}_{12}\text{O}_{33}$. *J. Solid State Chem.* 1:28–38
50. Wadsley AD, Andersson S. 1970. Crystallographic shear, and the niobium oxides and oxide fluorides in the composition region MX_x , $2.4 < x < 2.7$. In *Perspectives in Structural Chemistry*, Vol. 3, ed. JD Dunitz, JA Ibers, pp. 1–58. New York: Wiley
51. Anderson JS, Browne JM, Cheetham AK, Von Dreele R, Hutchison JL, et al. 1973. Point defects and extended defects in niobium oxides. *Nature* 243:81–83
52. Roberts MW, Thomas JM, Anderson JS, Tilley RJD. 1974. Crystallographic shear and non-stoichiometry. In *Surface and Defect Properties of Solids*, Vol. 3, ed. MW Roberts, JM Thomas, pp. 1–56. London: Chem. Soc.
53. Voskanyan AA, Abramchuk M, Navrotsky A. 2020. Entropy stabilization of $\text{TiO}_2\text{--Nb}_2\text{O}_5$ Wadsley–Roth shear phases and their prospects for lithium-ion battery anode materials. *Chem. Mater.* 32:5301–8
54. Bursill LA, Hyde BG, Philp DK. 1971. New crystallographic shear families derived from the rutile structure, and the possibility of continuous ordered solid solution. *Philos. Mag.* 23:1501–13
55. Bursill LA, Hyde BG. 1972. Crystallographic shear in the higher titanium oxides: structure, texture, mechanisms and thermodynamics. *Progr. Solid State Chem.* 7:177–253
56. Navrotsky A, Jamieson JC, Kleppa OJ. 1967. Enthalpy of transformation of a high-pressure polymorph of titanium dioxide to the rutile modification. *Science* 158:388–89
57. Watanabe D, Hirabayashi M, Ogawa S. 1955. On the superstructure of the alloy Cu_3Pd . *Acta Crystallogr.* 8:510–12
58. Caro PE, Corbett JD. 1969. Rare earth metal–metal halide systems. XII. The thulium–thulium(III) chloride system. Thulium(II) chloride and a series of intermediate phases. *J. Less Common Metals* 18:1–10
59. Abakumov AM, Handermann J, Bals S, Nikolaev IV, Antipov EV, Van Tendeloo. 2006. Crystallographic shear structures as a route to anion-deficient perovskites. *Angew. Chem. Int. Ed.* 45:6697–700
60. Abakumov AM, Handermann J, Van Tendeloo G, Antipov EV. 2008. Chemistry and structure of anion-deficient perovskites with translational interfaces. *J. Am. Ceram. Soc.* 91(6):1807–13
61. Abakumov AM, Handermann J, Batuk M, D'Hondt H, Tyablikov OA, et al. 2010. Slicing the perovskite structure with crystallographic shear planes: the $\text{A}_n\text{B}_n\text{O}_{3n-2}$ homologous series. *Inorg. Chem.* 49:9508–16
62. Abakumov AM, Batuk D, Handermann J, Rozova MG, Sheptyakov DV, et al. 2011. Antiferroelectric $(\text{Pb,Bi})_{1-x}\text{Fe}_{1+x}\text{O}_{3-y}$ perovskites modulated by crystallographic shear planes. *Chem. Mater.* 23:255–65
63. Batuk D, Batuk M, Abakumov AM, Tsirlin AA, McCammon C, et al. 2013. Effect of lone-electron-pair cations on the orientation of crystallographic shear planes in anion-deficient perovskites. *Inorg. Chem.* 52:10009–20
64. Canales-Vazquez J, Smith MJ, Zhou W, Irvine JTS. 2005. Studies on the reorganization of extended defects with increasing n in the perovskite-based $\text{La}_4\text{Sr}_{n-4}\text{Ti}_n\text{O}_{3n+2}$ series. *Adv. Funct. Mater.* 15:1000–8
65. Ruiz-Morales JC, Canales-Vazquez J, Savaniu C, Marrero-Lopez D, Zhou W, Irvine JTS. 2006. Disruption of extended defects in solid oxide fuel cell anodes for methane oxidation. *Nature* 439:568–71
66. Gado P. 1963. X-ray diffraction study of $\text{WO}_3\text{--W}_{20}\text{O}_{58}$ shear transformation. *Acta Crystallogr. A* 16:182
67. Gado P. 1965. X-ray powder diffraction study of the $\text{WO}_3\text{--W}_{20}\text{O}_{58}$ shear transformation. *Acta Phys. Hung.* 18:111–17

68. Anderson JS, Hyde BG. 1965. Dislocation mechanism for the production of Magnéli shear structures. *Bull. Soc. Chim. Fr.* 4:1215–16
69. Bursill LA. 1969. Crystallographic shear in molybdenum trioxide. *Proc. R. Soc. A* 311:267–90
70. Bursill LA, Hyde BG. 1969. Crystallographic shear in niobium oxyfluoride (NbO_2F). *Philos. Mag.* 20:657–63
71. Bursill LA. 1973. Direct observation of the formation of double-shear structures from $\text{Nb}_3\text{O}_7\text{F}$. *J. Solid State Chem.* 6:195–202
72. Bursill LA, Smith DJ. 1984. Interaction of small and extended defects in nonstoichiometric oxides. *Nature* 309:319–21
73. Andersson S, Wadsley AD. 1966. Crystallographic shear and diffusion paths in certain higher oxides of niobium, tungsten, molybdenum and titanium. *Nature* 211:581–83
74. O'Keeffe M. 1970. Discussion. In *The Chemistry of Extended Defects in Non-Metallic Solids*, ed. L Eyring, M O'Keeffe, pp. 374–78. Amsterdam: North Holland
75. Van Landuyt J, Amelinckx S. 1973. On the generation mechanism for shear planes in shear structures. *J. Solid State Chem.* 6:222–29
76. Merritt RR, Hyde BG. 1973. The thermodynamics of the titanium + oxygen system: an isothermal gravimetric study of the composition range Ti_3O_5 to TiO_2 at 1304 K. *Philos. Trans. R. Soc. A* 274:627–61
77. Catlow CRA. 1977. Point defect and electronic properties of uranium dioxide. *Proc. R. Soc. A* 353:533–61
78. Catlow CRA, James R. 1982. Disorder in TiO_{2-x} . *Proc. R. Soc. A* 384:157–73
79. Catlow CRA. 1981. Defect clustering in nonstoichiometric oxides. In *Nonstoichiometric Oxides*, ed. OT Sorensen, pp. 61–98. Orlando/London: Academic
80. James R, Catlow CRA. 1977. The energetics of shear plane formation in reduced TiO_2 . *J. Phys. Colloq.* 38:C7-32–35
81. Catlow CRA, James R. 1978. Non-stoichiometry and dielectric properties. *Nature* 272:603–5
82. Tilley RJD. 1977. Correlation between dielectric constant and defect structure of non-stoichiometric solids. *Nature* 269:229–30
83. Bérardan D, Franger S, Dragoe D, Meena AK, Dragoe N. 2016. Colossal dielectric constant in high entropy oxides. *Phys. Status Solid. RRL* 10:328–33
84. Baumard JF, Panis D, Anthony AM. 1977. A study of Ti-O system between Ti_3O_5 and TiO_2 at high temperature by means of electrical resistivity. *J. Solid State Chem.* 20:43–51
85. Stoneham AM, Durham PJ. 1973. The ordering of crystallographic shear planes: theory of regular arrays. *J. Phys. Chem. Solids* 74:2127–35
86. Iguchi E, Tilley RJD. 1977. The elastic strain energy of crystallographic shear planes in reduced tungsten trioxide. *Philos. Trans. R. Soc.* 286:55–85
87. Magnéli A. 1970. Structural order and disorder in oxides of transition metals of the titanium, vanadium and chromium groups. In *The Chemistry of Extended Defects in Non-Metallic Solids*, ed. L Eyring, M O'Keeffe, pp. 148–63. Amsterdam: North Holland
88. Cormack AN. 1982. Long range order in non-stoichiometric oxides. In *Computer Simulation of Solids*, ed. CRA Catlow, WC Mackrodt, pp. 302–11. Berlin/Heidelberg, Ger.: Springer
89. Prasanna TRS, Navrotsky A. 1994. Energetics in the brownmillerite-perovskite pseudobinary $\text{Ca}_2\text{Fe}_2\text{O}_5\text{-CaTiO}_3$. *J. Mater. Res.* 12:3121–24
90. Cheetham AK, Von Dreele BR. 1973. Cation distributions in niobium oxide block structures. *Nat. Phys. Sci.* 244:139–40
91. Rost CM, Sachet E, Borman T, Moballeghe A, Dickey EC, et al. 2015. Entropy-stabilized oxides. *Nat. Commun.* 6:8485
92. Sarkar A, Velasco L, Wang D, Wang Q, Talasila G, et al. 2018. High entropy oxides for reversible energy storage. *Nat. Commun.* 9:3400
93. Gild J, Samiee M, Braun JL, Harrington T, Vega H, et al. 2018. High-entropy fluorite oxides. *J. Eur. Ceram. Soc.* 38:3578–84
94. Jiang S, Hu T, Gild J, Zhou N, Nie J, et al. 2018. A new class of high-entropy perovskites. *Scr. Mater.* 142:116–20
95. Sarkar A, Breitung B, Hahn H. 2020. High entropy oxides: the role of entropy, enthalpy and synergy. *Scr. Mater.* 187:43–48

96. Navrotsky A, Kleppa OJ. 1967. The thermodynamics of cation distributions in simple spinels. *J. Inorg. Nucl. Chem.* 29:2701–14
97. Akaogi M, Navrotsky A. 1984. Calorimetric study of the stability of spinelloids in the system NiAl_2O_4 - Ni_2SiO_4 . *Phys. Chem. Miner.* 10:166–72
98. Evans HA, Wu Y, Seshadri R, Cheetham AK. 2020. Perovskite-related ReO_3 -type structures. *Nature* 5:196–213
99. Simonov A, De Baerdemaeker T, Bostrom HLB, Gomez MLR, Gray HJ, et al. 2020. Hidden diversity of vacancy networks in Prussian blue analogues. *Nature* 578:256–60
100. Jaffe A, Long JR. 2020. Ordered absences observed in porous framework materials. *Nature* 578:222–23